Abdasalam M. M. Eramah[1], Srđan Tadić[2], Aleksandar Sedmak[1]

IMPACT FRACTURE RESPONSE OF FRICTION STIR WELDED Al-Mg ALLOY

PONAŠANJE LEGURE Al-Mg FRIKCIONO ZAVARENE MEŠANJEM PRI UDARNOM LOMU

Naučni rad / Scientific paper
UDK /UDC: 669.715`721: 539.42
Rad primljen / Paper received: 17.12.2013

Adresa autora / Author's address:
[1)] University of Belgrade, Faculty of Mechanical Engineering, Belgrade, Serbia
[2)] Innovation Centre of the Faculty of Mechanical Engineering, Belgrade, Serbia

Keywords
- impact fracture
- ductile tearing
- crack initiation
- friction stir welding
- aluminium alloys

Ključne reči
- udarni lom
- duktilno čupanje
- inicijacija prsline
- frikciono zavarivanje mešanjem
- legure aluminijuma

Abstract

Effects of friction stir welding (FSW) variables on the Charpy impact fracture behaviour of Al-Mg 5083 alloy are investigated. Rotational and traversal welding rates are linked to the dynamic crack initiation and ductile tearing. The fracture mechanism is clarified by numerical and fractographic analysis. Results had revealed that initiation and stable crack propagation is not significantly influenced by the applied welding variables. It is attributed to the strain hardening of the investigated alloy. However, the final unstable phase of ductile tearing is strongly susceptible to the imperfections in the stirring zone of the weld

Izvod

Ispitivani su uticaji parametara frikcionog zavarivanja mešanjem na ponašanje loma udarom po Šarpiju u leguri Al-Mg 5083. Rotaciona i poprečna brzina zavarivanja su povezane sa dinamičkom inicijacijom prsline i duktilno čupanje. Mehanizam loma je razjašnjen numeričkom i fraktografskom analizom. Rezultati pokazuju da na inicijaciju i na stabilan rast prsline ne utiču toliko parametri postupka zavarivanja, koliko deformaciono ojačavanje ispitane legure. Međutim, konačna nestabilna faza duktilnom cepanja u velikoj meri zavisi od grešaka unutar zone mešanja u metalu šava.

INTRODUCTION

Friction stir welding (FSW) is a distinctive material joining technique invented by The Welding Institute (TWI) /1/. If properly conditioned, FSW can produce superior mechanical properties in the weld zone. Mostly applied to aluminium alloys, it has gradually become one of the most important joining processes within the last two decades. FSW has replaced conventional arc welding for aluminium alloys, even in some high-tech applications as are aeronautical and railway vehicles, /2/. Among the other benefits of this technology, FSW is a solid state process, consumes considerably less energy, neither shielding gas nor filler metals are used and it is considered to be a "green" technology, /3/.

In FSW, the rotating tool with a specially designed shoulder and pin is inserted into the edges of plates to be joined and moved along the line of joining. The most of the heat is generated between the tool shoulder and the surface of the work-pieces, /4/. Dissipated heat makes welding material pliable (without reaching the melting point) and allows travelling of the rotating tool along the welding line. Apart from generated heat, the tool serves to stir already softened material around the inserted pin. Proper adjustment of the generated heat flux (i.e. temperature) and stirring flow around the pin produce a welded joint. It is (or, perhaps, should be) the consequence of simultaneous rotational and transversal motion of the welding tool. But, other controllable parameters of the process are of great importance, such as shoulder and pin radius, tool tilt angle, tool pressure, stirrer geometry, toll design and so on. Good understanding of the thermal mechanics in the FSW process is of prime importance to produce a faultless joint, /5, 6, 7/. It has been a subject of numerous research investigations, and within the recent years, has resulted in huge amount of published literature. However, the process itself strongly depends on properties of particular material to be welded. It seems that material behaviour during FSW (which is basically hot working at elevated temperature, a kind of continual extrusion and forging on a micro-level) is the main variable that needs to be process-tailored.

The 5xxx series are magnesium strengthened alloys. In traditional welding techniques, these alloys are considered to be easily weldable with low crack sensitivity. The most prominent member from this family is the 5083 alloy with manganese and chromium as minor alloying elements. Typical application is in corrosive surroundings, marine structures, pressure vessels, transportation equipment etc. A distinctive feature of 5083 is to be a non heat-treatable, work-hardenable alloy. Accordingly, it should be expected to behave quite differently in comparison with other, heat treatable alloys during FSW. However, reports on mechanical properties of FSW 5xxx alloys are limited. A good review can be found in ref. /8/. When the fracture toughness is concerned, reported data are even more reduced. The objective of this paper is to inspect the impact response and

fracture behaviour of 5038 alloy. A series of friction stir welded specimens, varying rotational and traverse velocity of the welding tool, are subjected to impact fracture on the instrumented Charpy pendulum. Fracture behaviour, crack initiation and crack growth are discussed in terms of rotational (ω) and traverse (v) velocity in FSW.

EXPERIMENTAL

The base material is supplied as a 6 mm thick plate in the annealed (O-temper) condition. The nominal chemical composition of this alloy is 4–4.9% Mg, 0.4–1% Mn, 0.05–0.25% Cr, and the balance – Al. The plate is cut into 260 × 45 mm strips, whereas two strips make a single pair for FSW butt-joints. Before each welding experiment, every pair of strips is firmly clamped on the stainless steel backing plate.

Welding experiments are performed on a FSW-adapted laboratory milling cutter equipped with accurate displacement control, i.e., the depth of penetration, rotational and traverse speed are kept constant during the single welding cycle. The welding parameters are as follows: rotational velocity 500–800 rpm, traverse velocity 75–125 mm/min and tool-tilt-angle 1–4°. The tool, made of tool steel H13, had a φ = 25 mm shoulder and left threaded cone probe of 5.5 mm height.

To evaluate the impact behaviour of the friction stir weldments, the Charpy impact test notched specimens (CVN) are machined. Specimen size are 10 × 6 × 55 mm^3 with 45° V-notch of 2 mm depth and 0.25 mm root radius. These are subsized non-standard specimens whose dimensions are dictated by the thickness of the plate. Notches are machined at the rear side of the welding direction, precisely along the welding line of weldments.

Charpy impact tests are carried out at room temperature using instrumented impact pendulum. The pendulum is equipped with load cells positioned on a striker edge. The measuring device is connected to high-speed data acquisition with response time in terms of mili-seconds. The instrumented system enabled to collect instantaneous load and time data from pendulum during the "fracture opening time". Typical impact fracture time has lasted 2.6×10^{-3} seconds and, within this period, 2600 measuring points, load–time, are recorded into the accompanied digital oscilloscope. These digital signals are transferred into a personal computer for post-processing analysis of the fracture behaviour.

To understand the fracture behaviour, surfaces of fractured specimens are examined under JEOL JSM-3860 scanning electron microscope (SEM) and Nikon digital macro camera.

RESULTS AND DISCUSSION

Data obtained from the instrumented impact test is characterized with superimposed erratic oscillations. In order to smoothen the recorded signals, the method of moving averages /9/ is applied. The recursive procedure has been repeated until a distinguishable curve was produced. For reasons that shall be obvious later in the text, utmost care has been paid to precisely reveal the elastic part of the deformation. Only the extremely sharp peaks are removed. To determine the load-displacement curve, displacement (d) is calculated by the following equation, /10/:

$$d(t) = \int_{t_0}^{t} v(t)dt \tag{1}$$

where the $v(t)$ is the time-dependent velocity of the impact hammer given by:

$$v(t) = v_0 - \frac{g}{m}\int_{t_0}^{t} F(t)dt \tag{2}$$

where m and v_0 are mass and initial velocity of the impact hammer (5.17 m/sec). Numerical integrations are performed by trapezoidal rule with linear interpolation between successive data points.

Curves of calculated force vs. displacement are shown in Figs. 1(a-f). For the purpose of comparison, the figures are arranged in a following manner: on the left (Figs. 1a, c, d) are curves belonging to γ = 75 mm/min traverse speed with rotational speed ω = 600, 700 and 800 rpm; on the right are γ=125 mm/min curves, with the corresponding specified rotational speeds. In terms of heat input, which is proportional to ω/v ratio, the left and right column of figures might be considered as a 'high-' and 'low-heat-input' welded joints. (i.e., where 'high' and 'low' should be regarded in relative sense). Although still settled with oscillations, the general flow of the curves (and noticeable dissimilarities among them) can be easily observed. Curves are subjected to the least squares analysis in segments of elastic and plastic deformation. Elastic segments of the deformation are fitted by linear, first order function. Results of these analyses are inserted into the figures in the form $F_{el} = a + b \times d_{el}$, where F_{el} and d_{el} are elastic-domain-load and d_{el} is corresponding displacement, (reader may notice that the reciprocal of b refers to the value of elastic compliance). In a similar way, plastic segments, up to the apparent maximal force, are fitted by cubic equation. While it may look a bit trivial, the choice of the fitting equation seems to be of prime importance. Second-order and cubic spline are also inspected, but the third order polynomial fit has shown to be optimal, as it can be deduced in Figs. 1(a, c, d). However, in 'low-heat-input' curves, Figs. 1(b, d, f), at the very beginning of plastic segment deformation, a kind of 'pianoline' can be noticed. It isn't quite clear does it indeed reflect some strain hardening phenomena in the beginning of plastic deformation or, simply, is an artificial result of the cubic fit. Later in this text, the parabolic normalization shall be introduced.

The beginning of plastic deformation is determined as the load at the intersection of elastic and plastic segments of load-deflection curves. Dynamic yield stress, σ_{ys}, is calculated from /11/:

$$\sigma_{ys} = \frac{2.99F_{ys}W}{Bb_0^2} \tag{3}$$

where W, B and b_0 are width, thickness and initial ligament of CVN specimens. Inspection of Figs. 1 reveals that for all specimens F_{ys} is very close to 2.5 kN, (a more significant exception is noticeable only in Fig. 1e, where F_{ys} = 2.8 kN).

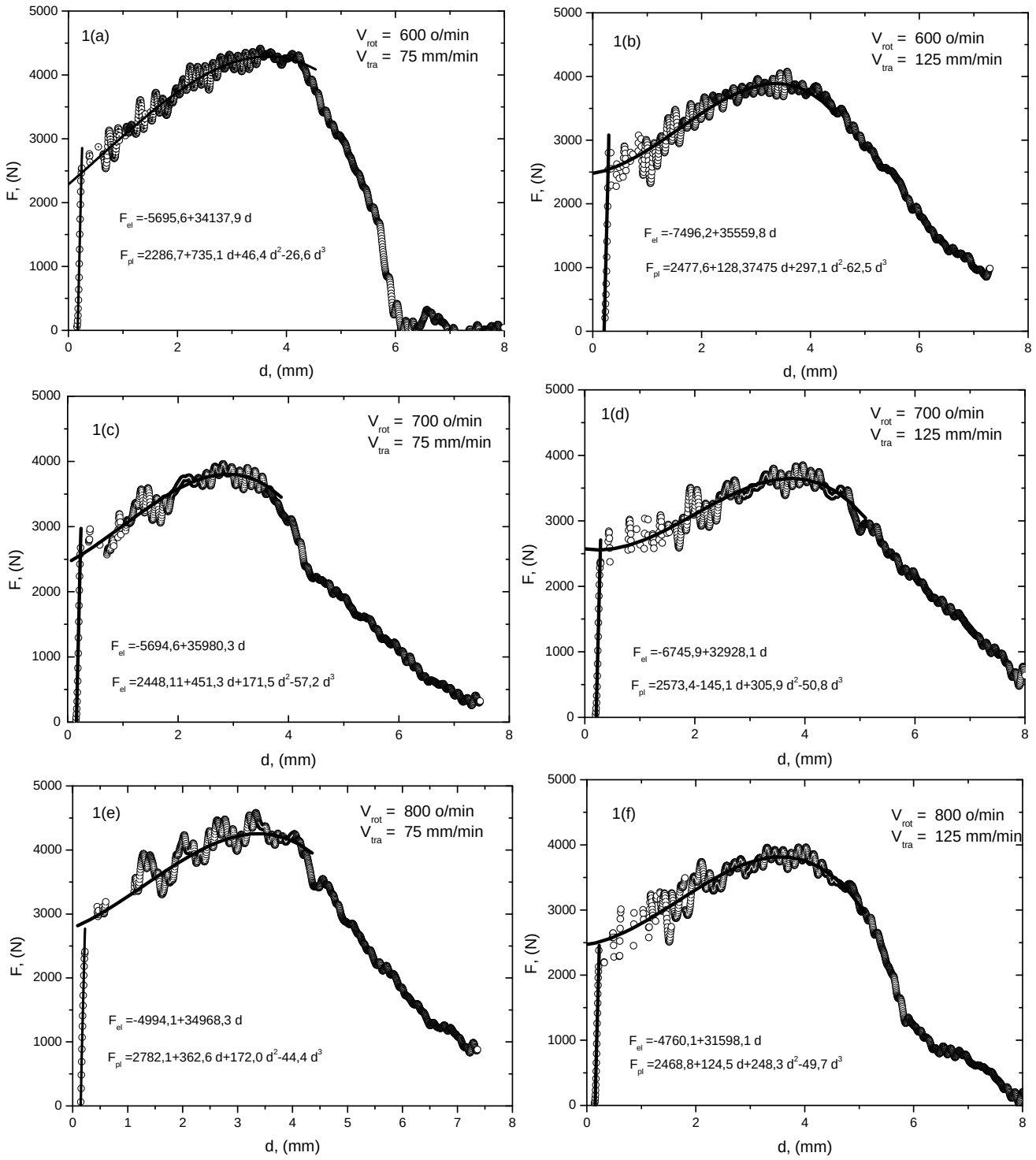

Figure 1(a-f). Load–deflection curves of the investigated specimens.
Slika 1(a-f). Krive opterećenje–pomeranje ispitivanih epruveta

Applying Eq. (3) the dynamic yield stress is σ_{ys} = 195 MPa. Calculated values of dynamic yield stress had resolved that within the reasonably narrow scatter, σ_{ys} is not affected by FSW (at least in the range of the applied FSW parameters). Perhaps a surprising observation, it can be rationalized in the sense of the fact that the investigated alloy is a non-heat-treatable work hardenable alloy. On this account, and recalling that σ_{ys} is the stress at the very beginning of plastic deformation, this can explain the behaviour of the dynamic yield stress. However, it would be of great interest if this result might be confirmed by standard tensile test.

In ductile materials, the compliance changing rate method, /12/, has been demonstrated to be reliable for detecting the crack initiation point. The compliance changing rate is given as

$$\frac{\Delta C}{C} = \frac{C - C_{el}}{C_{el}} \tag{4}$$

where the compliance C refers to the plastic segment of the load-deflection curve $C = dd/dF$. According to this method, in a plot $\Delta C/C$ vs. deflection, a rapid change of the slope indicates crack initiation. Although it might not be obvious from the equation, this is ingeniously connected with the rapid decreasing of specimen cross-section. The application of the compliance rate method is illustrated in Fig. 2(a, b), (where the compliance change rate refers to the right y-axes). Arrows denote deflection at F_{max} and, before the maximal load, the compliance-calculated deflection at the crack initiation. Examination of all curves has revealed that deflection at the crack initiation point is about 0.6 mm less than the F_{max} deflection, i.e., $d_{(crack)} \approx d_{(F max)} - 0.6$. Only one exception is found where $d_{(crack)}$ and $d_{(F max)}$ are almost identical.

Once the dynamic crack initiation is created in the ductile material, the stable plastic tearing due to crack growth follows. Typically, a contribution of stable plastic tearing energy to the total fracture energy, E_{pl}/E_t, defines the mode of fracture. This fracture period spans from crack initiation point up to the point 'a bit beyond' the F_{max}. In order to determine the stable crack period, instantaneous fracture energy is recalculated as a function of deflection, Fig. 3(a, b). Typical s-curves are obtained where the linear segment defines stable crack growth. Figures depict critical points of fracture propagation in terms of consumed fracture energy vs. deflection: crack initiation (from the compliance method), maximal load energy, and at the point where the curve deviates from linearity – the beginning of the so-called unstable crack growth. Finally, the curve asymptotically reaches the total fracture energy. The reader might notice quite different behaviour in the slope of the unstable crack growth period. From this behaviour it might be concluded that the 'high-heat' curve (Fig. 3b) is more ductile than the 'low-heat' (Fig. 3a) curve. However, the total facture energy, as well as stable crack growth energy are almost the same. This might implicitly lead to the conclusion that FSW (namely-heat input from the applied welding parameters) mostly affects the final, unstable crack propagation.

To further examine the above assumption, a normalization method /13, 14/ and a key-curve method /15, 16/ have been applied in the present analysis. Generally, these methods are used as a so-called 'single specimen methods' to calculate J-values and are validated in a large number of various materials and crack geometries, /17/. However, in

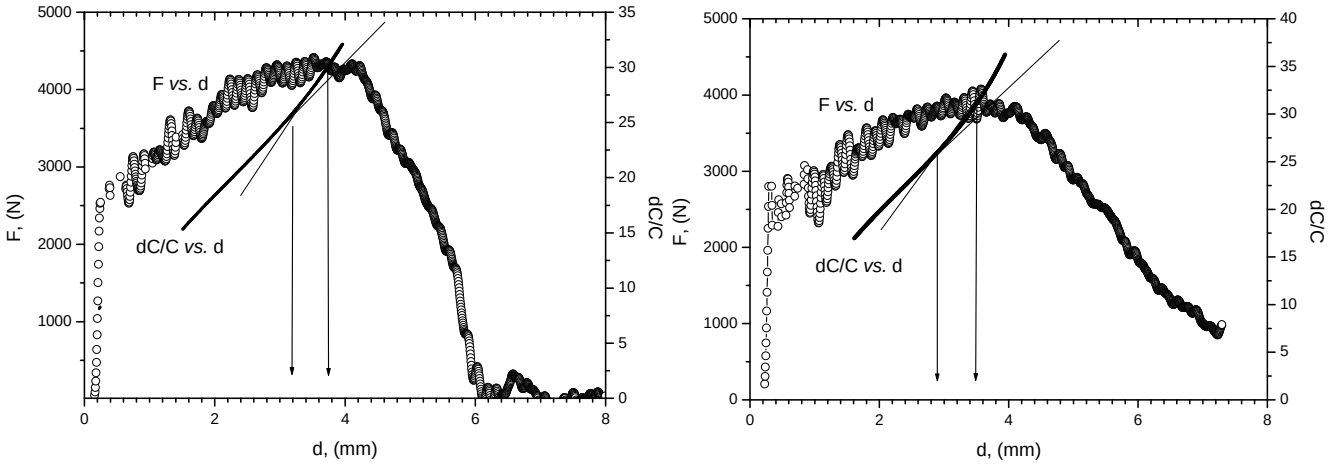

Figure 2(a, b). Compliance of initial crack determination.
Slika 2(a, b). Poklapanje u određivanje inicijacije prsline

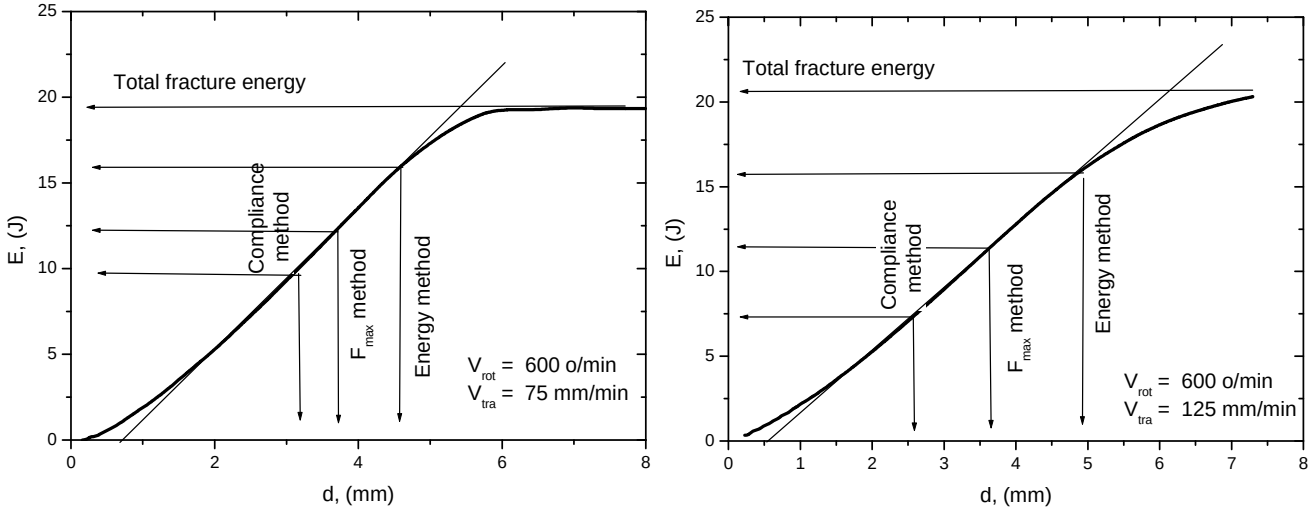

Figure 3(a, b). Fracture energy as a function of deflection.
Slika 3(a, b). Energija loma u funkciji ugiba

this paper, only the crack growth, Δa, shall be processed. Principally, load-deflection data, starting after yielding up to the previously estimated crack initiation, are fitted to the power law equation

$$\frac{FW}{b_0^2} = K\left(\frac{d_{pl} - C_{el}F_{el}}{W}\right)^n \tag{5}$$

with F and d meaning load and deflection, W–width (10 mm) and b_0 – initial ligament width ($W - a_0 = 8$ mm in this work) of the specimens. Coefficients K and n can be easily calculated in a double-logarithmic plot by linear least squares analysis. Once the K and n are determined, crack growth can be introduced by

$$\Delta a = (W - a_0) - \sqrt{\frac{F}{K}\frac{W^{n+1}}{d^n}} \tag{6}$$

From the above equation, crack extension Δa can be estimated to any deflection on the load-deflection curve, from crack initiation up to the beginning of unstable crack growth. The procedure, if carefully managed, enables to estimate the initial dynamic crack length. Relations between crack extension and deflection in the two illustrated examples are shown in Fig. 4. Quite different behaviour can be seen from high- and low-heat-input specimens. This is also revealed in all the rest of the examined specimens. It probably can be connected with the strain-hardening behaviour, which is implicitly introduced as the n-coefficient of Eq.(5). In particular, the n-coefficients of the high-heat curves are much higher than those of low-heat, on an average – 0.24 vs. 0.19. Explicitly, the lesser n-value (i.e. strain hardening), the steeper is the Δa dependence on deflection. But, in all of the calculated curves, the initial dynamic crack length yields a narrow span $\Delta a_0 = 0.3 - 0.5$ mm. Consumption of fracture energy during the crack extension is shown in Fig. 5. Also, in the same figure, the rate of energy per crack extension $dE/\Delta a$ vs. Δa is also shown. Almost identical curves are acquired. The very similar behaviour, within the narrow scatter band, has been given for other examined specimens.

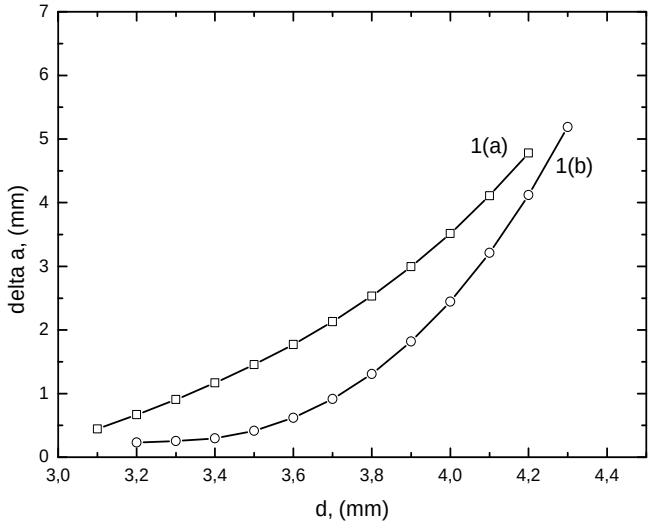

Figure 4. Δa extension vs. deflection.
Slika 4. Δa rast u zavisnosti od ugiba

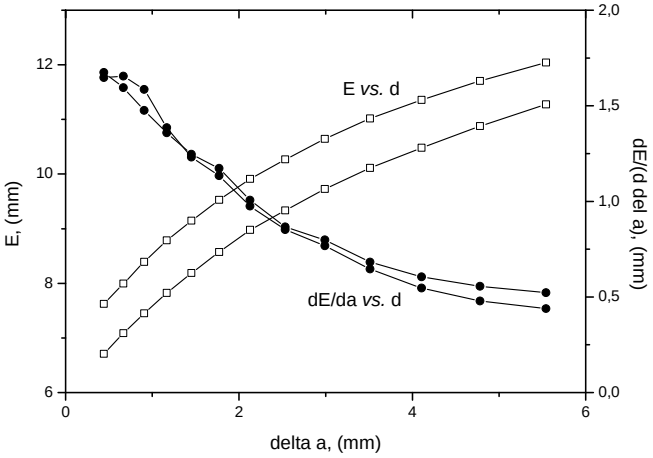

Figure 5. Energy and energy rate per Δa.
Slika 5. Energija i brzina promene energije u funkciji Δa

To reach further insight into the fracture behaviour, scanning electron microscopy (SEM) has been utilized for fractographic characterization. The objectives of SEM examinations are (*i*) to get closer aspects of the failure mode of the fractured specimens and, (*ii*) to inspect the validity of the numerical procedure depicted in Eqs.(5) and (6). Representative examples of several hundreds of SEM fractographic inspections are shown in Figs. 6–11. Low-magnification SEM fracture images are presented in Figs. 6 and 7. These specimens are the same ones whose load-deflection curves are shown in Fig. 1(a, b). The reader might notice machined notches at the upper side of images. The FSW tool has been stirring on the left-side surfaces, in a downward direction. The outlined zone at the left side (zone *a*) is a 'lever arm' zone, mostly affected by heat generated through the tool shoulder. At the right side, zone *b*, is the bottom of the stirring zone, affected by the top of the tool pin. This surface is clamped onto the stainless steel back plate. However, these zones are also affected by the final stage of failure – formation of shear lips. At the root of the notches encircled are initial dynamic crack zones. These segments enlarged are shown in Figs. 8, 9. The length of the initial crack seems to be in excellent agreement, Δa =0.3–0.5 mm, calculated by Eqs. (5) and (6). Also, in these figures, the initial points of cracks are marked by arrows.

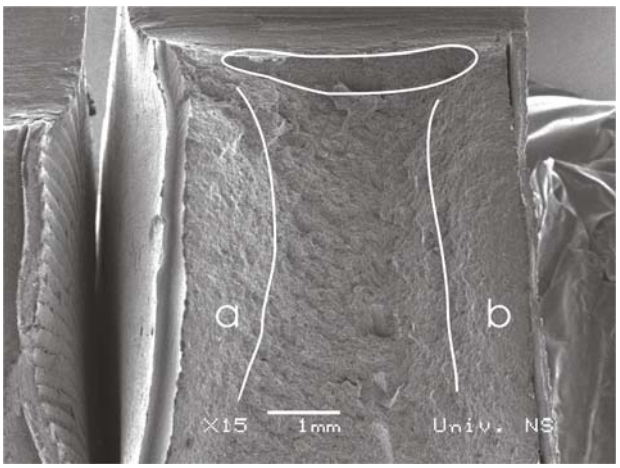

Figure 6. Low-magnification SEM of the 1(a) curve.
Slika 6. SEM - Slabo uvećanje krive 1(a).

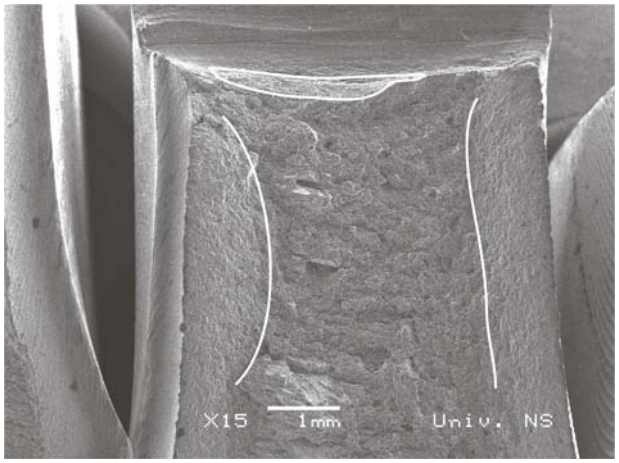

Figure 7. Low-magnification SEM of the 1(b) curve.
Slika 7. SEM - Slabo uvećanje krive 1(b)

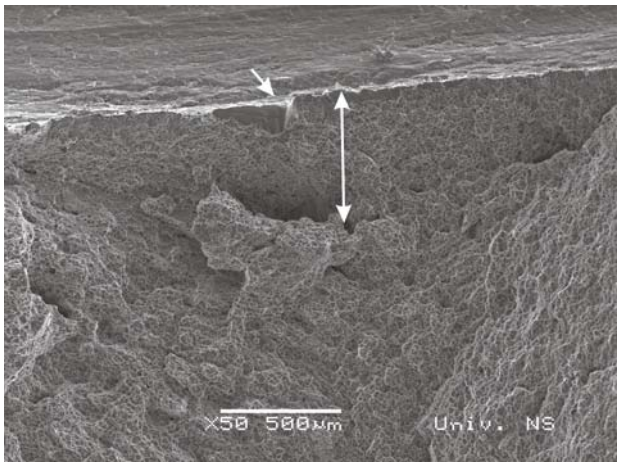

Figure 8. Crack initiation in the 1(a) curve.
Slika 8. Inicijacija prsline kod krive 1(a)

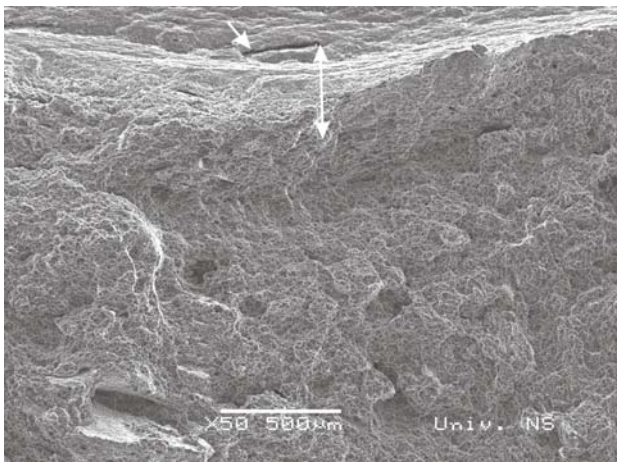

Figure 9. Crack initiation in the 1(b) curve.
Slika 9. Inicijacija prsline kod krive 1(b)

Once the initial crack growth reaches a critical value, ductile plastic tearing takes place, propagating into the mid-section of the specimens that is mostly affected by stirring flow around the pin. The image of the fractured surface in the stirring zone (Fig. 10) appears to be a typical ductile tearing. Dimples of different sizes with precipitates at bottom, make the fracture highly ductile. Around larger

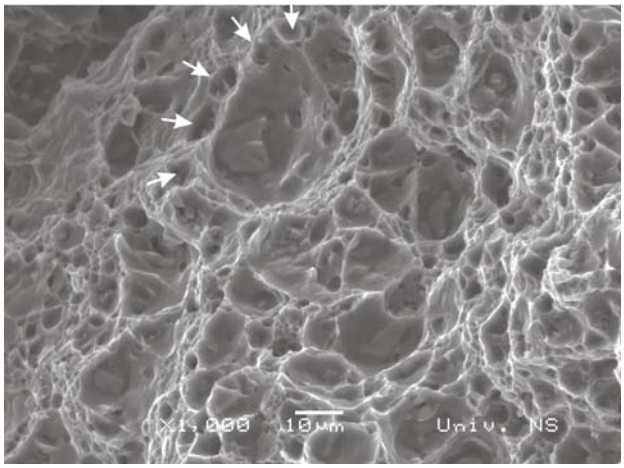

Figure 10. Dimples of the fracture surface.
Slika 10. Jamice na površini preloma

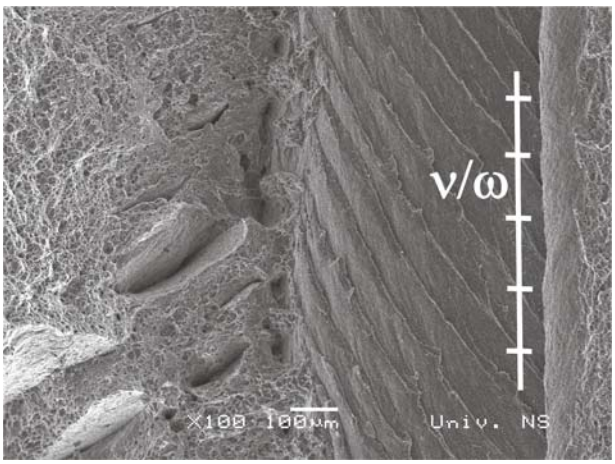

Figure 11. Worm-holes and onion-rings.
Slika 11. Crvotočine i prsteni

dimples (10-30 μm), second generation dimples, in a necklace formation (marked by arrows) can be seen. This failure mechanism, often referred to as 'void sheeting', is connected to low stress tri-axialities, /18/. A distinctive feature of the fracture surface is represented by high tearing ridges between voids – a sign of intensive plastic deformation during crack propagation, /19/. Accordingly, the propagation of the crack requires a consumption of large energy (on behalf of the plastic deformation of tearing ridges), an observation that is consistent with analysis of the impact curves. Finally, within certain FSW conditions, an incomplete, partial consolidation of the material can occur. It is shown in Fig. 11, where the stirred material in this zone is consolidated in a discontinuous manner, leaving in-between tunnels (or 'worm-holes' that are closely related to low vertical pressure of the welding tool, /20/). This is the zone of fast fracture. The size and distribution of worm-holes reflects the stepwise, bouncing behaviour on the right side of the load-deflection curves from Fig. 1. It can be easily imagined that during ductile tearing, crack growth is discontinuously interrupted by numbers of worm-holes which effectively, reduce cross sectional area of the impact specimen. Depending on the size and distribution of warm-holes, fast fracture can occur as a sequential series of plastic tearing and worm-hole opening phases. But, to avoid specu-

lations, a more sensitive experimental method is required to fully expand the presented assumptions. Regarding Fig. 11, worm-holes are closely related to 'onion-rings' phenomena, /21/, which can be seen on the right side of the image, as a series of concentric equally spaced striations. The distance between successive striations is $d = v/\omega$ or, simply, it is the tool advance per rotation, /22/. However, the connection between onion rings and worm-holes is not quite clear. Anyhow, it is beyond the scope of this paper and shall be elaborated in one of the succeeding papers.

CONCLUSIONS

Results presented in this paper concern impact fracture behaviour of friction stir welded Al-Mg 5083 alloy. Experimental results are focused onto Charpy impact testing and SEM examinations. Numerical normalization and key-curve methods are utilized to estimate the crack initiation and extension during the fracture opening. Reasonable accordance is found when dynamic crack initiation is concerned. Ductile, high energy fracture behaviour is found to be driven by high strain hardening of the alloy. Finally, the fast fracture stage of tearing is found to be extremely dependent on the stirring zone imperfections.

ACKNOWLEDGEMENTS

This work is supported by the Serbian Ministry of Education, Science and Technological Development. The authors are grateful to Dr A. Živković for FSW experiments and to Prof. Dr K.Gerić for SEM-spent-time. Charpy tests are performed at the Military Institute in Žarkovo.

REFERENCES

1. Thomas, W.M., et al., *Friction stir butt welding*, International Patent Application, PCT/GB92/02203, December 1991.
2. Thomas, W.M., Nicholas, E.D., Materials & Design, Vol.18, 1997, p.269.
3. Threadgill, P.L., Friction Stir Welding – State of The Art, TWI report-678/1999.
4. Nandan, R., Roy, G.G., Debroy, T., Acta Mater., 55, 2007, p.883.
5. Schmidt, H.N.B., Dickerson, T.L., Hattel, J.H., Acta Mater., 54, 2006., p.1199.
6. Grujicic, M., et al., J of Mat. Eng. and Perf., 20, 2011, p.11.
7. Rhodes, C.G., Mahoney, M.W., Bingel, W.H., Scr. Mat., 36., 1997, p.69.
8. Mishra, R.S., Mahoney, M.M., Friction Stir Welding and Processing, ASM, 2007.
9. Kobayashi, T., Eng. Fract. Mech. 19(1), 1984, p.49.
10. Chaouadi, R., J of Test. and Eval., 32, No.6, 2004, p.469.
11. Sreenivasan, P.R. et al., Eng. Fract. Mech. 42(6), 1992, p.1047.
12. Kobayashi, T., Yamamoto, T., J of Test. and Eval. 21(3), 1993, p.145.
13. Herrera, R., Landes, J.D., *Direct J -R curve methodology: a guide to the methodology*, Edited by J.P. Gudas, J.A. Joyce and E.M. Hackett, ASTM, Philadelphia, PA, 24-43.
14. Zhu, X., Joyce, J., Eng. Fract. Mech., 74, 2007, p.2263.
15. Hernando, C., et al., Int. J of Fract., 117, 2002, p.247.
16. Joyce, J., et al., Fatigue anf Fracture Mechanics, ASTM Philadelphia, 2001.
17. Sreenivasan, P.R., Mannan, S.L., Int. J of Fract., 101, 2000, p.229.
18. Thomason, P.F., Fatigue & Fract. of Eng. Mat. & Struct., 21, 1998, p.1105.
19. Besson, J., *Continuum Models of Ductile Fracture: A Review*, Int. J of Damage Mech., 19, 2010, p.19.
20. Kim, Y.G., et al., Mat. Science and Engng. A415, 2006, p.250.
21. Krishnan, K.N., Mat. Science and Engng. A327, 2002, p.246.
22. Cui, G.R., Ma, Z.Y., Li, S.X., Scripta Materialia, 58, 2008, p.1082.